



Cite this: *J. Mater. Chem. C*, 2016, **4**, 7577

## Thermal pressing of a metal-grid transparent electrode into a plastic substrate for flexible electronic devices†

Youngwoo Lee,<sup>‡a</sup> Won-Yong Jin,<sup>‡b</sup> Kuk Young Cho,<sup>c</sup> Jae-Wook Kang<sup>\*b</sup> and Jihoon Kim<sup>\*a</sup>

A flexible transparent electrode (TE) is fabricated by thermal pressing of a metal-grid into a plastic film. The metal-grid is prepared by electrohydrodynamic continuous jet printing, which easily provides a high aspect ratio for the printed lines. Embedding the high-aspect-ratio metal-grid results in a smooth surface morphology that promotes the uniform deposition of functional materials over the metal-grid TE. The thermal-pressed metal-grid TEs show excellent electrical and optical performance: a sheet resistance of  $0.5 \Omega \text{ sq}^{-1}$  and an optical transmittance above 80% lead to a figure of merit of 2000. The flexibility of the thermal-pressed metal-grid TE is investigated under both compressive and tensile bending stresses. Invariant electrical performance is observed for a bending radius of up to 3 mm. Less than 30% degradation of the original electrical performance occurs after 1000 compressive–bending cycles with a radius of 10 mm. Organic solar cells fabricated on the thermal-pressed metal-grid TEs demonstrate acceptable device performance equivalent to devices fabricated on commercial indium tin oxide glass. These properties confirm the feasibility of thermal-pressed metal-grid TEs for use in flexible electronics.

Received 24th March 2016,  
Accepted 17th July 2016

DOI: 10.1039/c6tc01234e

www.rsc.org/MaterialsC

## Introduction

A transparent electrode (TE) is one of the required components in a wide range of optoelectronic applications covering photo-voltaic cells, organic light-emitting diodes, and touch screen panels.<sup>1–7</sup> Conventionally, metal-oxide-based TEs with suitable doping elements, such as indium oxides doped with tin (ITO), have been widely used due to their reasonably high optical and electrical performance. However, ITO has several drawbacks, that hinder its application in future flexible electronics, such as its fragile nature, which can easily lead to crack-formation under bending stresses, and its high fabrication cost because of the scarcity of indium and its expensive vacuum-based fabrication processes.<sup>8–10</sup>

Recently, the technical issues associated with ITO have expedited a significant amount of research effort in exploring

alternative TEs; these TEs can be categorized into three groups, *i.e.* carbon-based TEs (such as carbon nanotubes, graphene films, and conducting polymers), metal-based TEs (such as metal nanowires and metal-grid electrodes) and hybrid-structure TEs (combination of carbon- and metal-based TEs). However, the performance of carbon-based TEs, especially when prepared by a solution-based process, is still below the conductivity and stability requirements for future flexible electronics.<sup>11–19</sup> In contrast, metal-based TEs, such as metal-grids and metal-nanowire networks, offer promising performance, being superior to ITO in terms of both conductivity and transmittance, along with reasonable flexibility. In particular, metal-grid TEs have gained prominence in both academia and industry for use in flexible electronics because they offer advantages over other alternative TEs *viz.* (a) easy management of electrical and optical properties by modulating the grid pitch, width, and thickness and (b) a decrease in fabrication cost because of their compatibility with printing technologies, which contributes to the efficient use of materials, a simple fabrication process, easy scalability to large-area applications, *etc.*<sup>19–22</sup> The fabrication of metal-grid TEs has been demonstrated by many researchers using various fabrication processes such as selective laser sintering, evaporative assembly, roll-offset printing, electroless plating, photolithography, electrohydrodynamic (EHD) jet printing, inkjet printing, and electrospinning.<sup>19,22–31</sup> It should be also mentioned that there is an effort to exploit the hybrid structure

<sup>a</sup> Division of Advanced Materials Engineering, Kongju National University, Cheonan-daero, Seobuk-gu, Cheonan, Chungnam, 31080, Korea.  
E-mail: jihoon.kim@kongju.ac.kr

<sup>b</sup> Department of Flexible and Printable Electronics, Polymer Materials Fusion Research Center, Chonbuk National University, Jeonju, 54896, Korea.  
E-mail: jwkang@jbnu.ac.kr

<sup>c</sup> Department of Materials Science and Chemical Engineering, Hanyang University, Ansan, Gyeonggi-do, 15588, Korea

† Electronic supplementary information (ESI) available. See DOI: 10.1039/c6tc01234e

‡ These authors contributed equally.

**Table 1** Dimensional, electrical, and optical properties of various metal-grid transparent electrodes. The sheet resistance ( $R_s$ ) in this table corresponds to the values for the transmittance ( $T$ ) greater than 80% or applied to the device fabrication. Please note that the transmittance values in the references are measured with and without a substrate. For a fair comparison, both transmittance values measured with and without substrates are presented for the thermal-pressed MGETEs

Process	Metal-grid location	Line height/width ( $\mu\text{m}$ )	Aspect ratio	$R_s$ ( $\Omega \text{ sq}^{-1}$ )	$T$ (%)
Selective laser sintering <sup>23</sup>	On surface	0.13/11	0.011	30	85 (w/Sub.)
Evaporative assembly <sup>22</sup>	On surface	0.09/4.5	0.020	97	92 (w/o Sub.)
Roll-offset printing <sup>24</sup>	On surface	0.3/20	0.015	12.9	85 (w/Sub.)
EHD printing <sup>19</sup>	On surface	1.5/7.5	0.200	9	85 (w/Sub.)
Inkjet printing <sup>27</sup>	On surface	0.2/50	0.004	10.3	73 (w/Sub.)
Electroless plating <sup>25</sup>	On surface	0.25/30	0.008	8.2	91 (w/o Sub.)
Photolithography <sup>31</sup>	On surface	0.03/5	0.006	9.1	79 (w/Sub.)
UV lithography <sup>26</sup>	On surface	0.05/15	0.003	51.4	76 (w/Sub.)
Direct imprinting <sup>34</sup>	Embedded	2.1/4.1	0.512	4.7	93 (w/o Sub.)
Gravure offset <sup>35</sup> (damascene process)	Embedded	1.3/39	0.033	13	93 (w/o Sub.)
Roll-to-roll thermal imprinting <sup>36</sup>	Embedded	1/10	0.100	6.8	80 (w/Sub.)
Thermal-pressing (this work)	Embedded	1.2/9.6	0.125	1.2	82 (w/Sub.) 94 (w/o Sub.)

of carbon- and metal-based TEs, presenting reasonable performance complementing the weaknesses of each other.<sup>32,33</sup>

The dimensional, electrical, and optical information on these pre-explored metal-grid TEs is summarized in Table 1. The pre-explored metal-grid TEs in Table 1 demonstrate satisfactory performance in terms of electrical and optical properties. However, for the realization of the next generation of flexible and large-area electronics, improved electrical and optical TE performance is required. A higher aspect ratio (AR, defined as thickness/width of the metal-grid line) may be a simple solution to this technical challenge for metal-grid TEs. However, the active layers in organic devices that are fabricated on metal-grid TEs are typically less than a few hundred nanometers thick. An increase of the AR with increasing thickness leads to a non-uniform surface morphology that prevents the active layers from being uniformly formed on the TEs. The non-uniform surface can cause degraded operation for organic devices or an easy electrical short-circuit between the metal-grid TE and a top electrode. In order to secure metal-grid TEs with both a high AR and a smooth surface morphology, the concept of embedding the metal-grid into a plastic substrate has been suggested by several research groups. Metal-grid-embedded TEs (MGETEs) were fabricated in two different fabrication schemes, as follows: (a) a metal-grid was formed onto a rigid substrate using a printing process, such as imprinting or gravure offset printing, followed by transferring the metal-grid into a plastic substrate,<sup>34,35</sup> and (b) grid-patterned trench lines were formed in a plastic substrate and filled with metal paste or ink using a printing process.<sup>36</sup> The performance of these MGETEs is also presented in Table 1. The value of the AR reaches 0.51 in the case of the MGETE. However, it is worth noting that the sheet resistance does not decrease with increasing AR in MGETEs compared to the metal-grid-on-surface TEs. This is attributed to the embedded metal-grid annealing inside the plastic substrates. It imposes a limitation on the annealing temperature, leading to no significant improvement in the electrical properties of the MGETE.

In this study, we demonstrate the fabrication of MGETEs in a simple and effective process. The metal-grid was directly patterned on top of a polyether sulfone (PES) plastic substrate

by EHD continuous jet printing and then thermal-pressed into the plastic substrate. Our new process reduces the overall process complexity and achieves a lower sheet resistance with a higher AR compared to the pre-explored MGETEs (a sheet resistance of less than  $1 \Omega \text{ sq}^{-1}$  with an AR greater than 0.12). The electrical and optical properties of the thermal-pressed MGETEs were investigated by modulating the metal-grid pitch. The flexibility of the MGETEs was examined by a bending test, showing no degradation up to a bending radius of 2 mm. The MGETEs with the optimum electrical and optical properties were then employed to fabricate flexible organic solar cells (OSCs), for which the performance is equivalent to that of OSCs on commercial ITO glass.

## Results and discussion

The schematic diagram for the fabrication of the thermal-pressed MGETEs is illustrated in Fig. 1. A metal-grid with a high AR was prepared on the PES plastic substrate by EHD jet printing. The high AR in the MGETEs originated because the EHD jet printing can print relatively high viscosity ink with a high solid concentration. The electric field applied to the EHD nozzle results in elongated streaming of the ink on the tip of the nozzle. The dimension of the ejected ink stream becomes

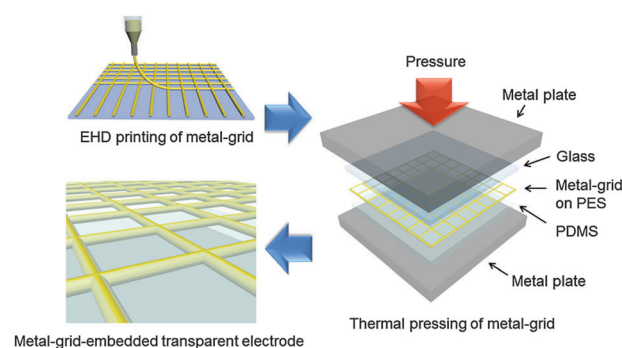


**Fig. 1** Schematic diagram for the fabrication of thermal-pressed metal-grid-embedded transparent electrodes.

much smaller than the diameter of the nozzle. The fine stream of the ink was used to print a metal-grid onto the plastic substrate with a relatively high AR (line width and thickness less than 10  $\mu\text{m}$  and 2  $\mu\text{m}$ , respectively). Further details on the EHD jet printing can be found in previous reports published by one of the authors.<sup>19,37</sup> The plastic substrate with the printed metal-grid was located between two metal plates. Two different buffer layers were introduced to both sides of the PES plastic substrate: a glass plate for the side with the metal-grid and a polydimethylsiloxane (PDMS) film for the other side of the plastic substrate. A constant pressure was applied to the metal plates and an adjustable mounting clip held the layers together. The pressure was fixed at 1.5 MPa during the experiment. The pressure was determined by monitoring the quality of the embedded metal-grid at various pressures (see Fig. S1 in the ESI†). The mounted sample unit was placed in a box furnace at various temperatures. A surface profilometer monitored the embedment of the metal-grid into the plastic substrate after the heat treatment. Fig. 2 shows the height of the metal-grid from the surface of the plastic substrate at different temperatures. The initial thickness of the printed metal-grid was 1.7  $\mu\text{m}$ . The height of the metal-grid decreased with increasing furnace temperature. Almost all of the metal-grids were embedded into the plastic substrate at a temperature close to the glass transition of the plastic substrate (PES:  $T_g = 230^\circ\text{C}$ ) where the height was measured to be less than 50 nm. The inset in Fig. 2 presents the surface profile of a metal line in the metal-grid before and after the thermal pressing at 230  $^\circ\text{C}$ . It was observed that the final line height decreased by 0.4 to 0.6  $\mu\text{m}$  after a full embedding of the metal grid.

The electrical properties of the MGETE were investigated after the thermal pressing at various temperatures ranging from 180  $^\circ\text{C}$  to 240  $^\circ\text{C}$ . During the thermal process, a separate sample that had the metal-grid TE printed on the glass substrate (reference sample) was heat-treated along with the MGETE samples in the same furnace. The pitch in both the MGETE and reference samples was fixed at 200  $\mu\text{m}$  for comparison. The difference in the

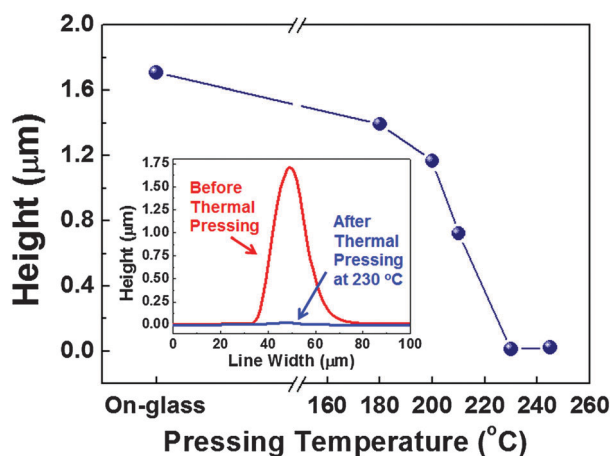


Fig. 2 Height of the metal-grid after pressing at various temperatures. The inset indicates the surface profile of a metal line before and after the thermal pressing at 230  $^\circ\text{C}$ .

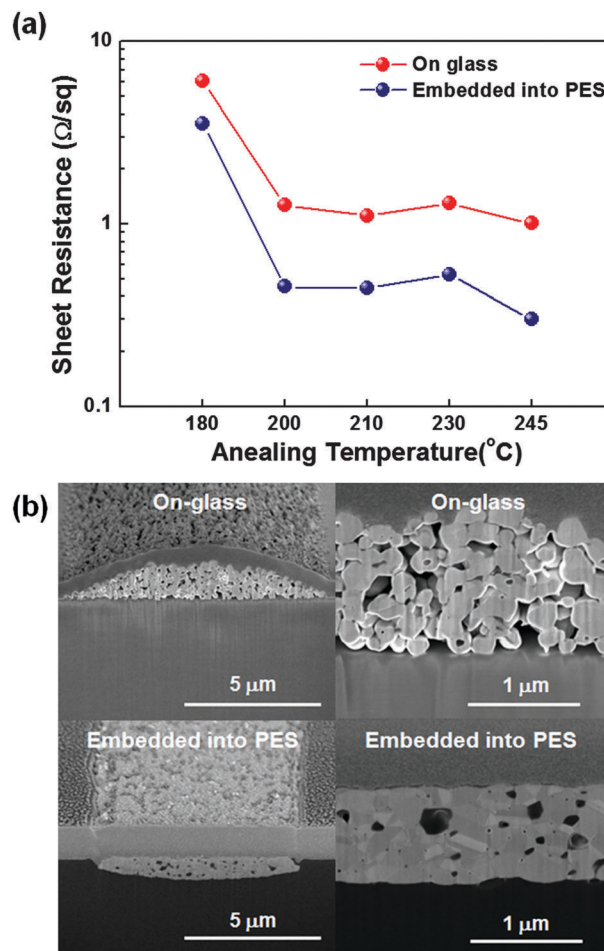


Fig. 3 (a) Difference in the sheet resistance of the MGETEs and reference samples. (b) Cross-sectional images of a metal line in the reference sample (on glass) and the thermal-pressed MGETE (embedded into PES) obtained by a focused-ion-beam field emission scanning electron microscope (FIB FESEM). The microstructure of each line is zoomed on the right column of the images. The tilt angle was 52 $^\circ$ .

sheet resistances between the MGETEs and the reference samples are plotted in Fig. 3(a). The sheet resistance of MGETE was almost one order of magnitude smaller than that of the reference sample, indicating a significant influence of the embedding process on the electrical properties of the metal-grid. The microstructures of both metal-grids, which were embedded into the plastic substrate and printed on the glass substrate, respectively, were analyzed by focused-ion-beam field emission scanning electron microscopy (FIB FESEM) to understand the difference in the sheet resistance. Fig. 3(b) shows cross-sectional images of the metal line in the MGETE and the reference samples. Ag particles in the MGETE were completely sintered and formed a dense microstructure with distinct grains, while the microstructure of the reference sample remained as Ag particles that were not fully sintered. These microstructures explain why there is a difference in the sheet resistance between the MGETE and the reference samples. The MGETEs pressed at temperatures above 200  $^\circ\text{C}$  had a sheet resistance less than 0.5  $\Omega\text{sq}^{-1}$ , which is one of the lowest values reported for metal-grid based TEs prepared using various methods.



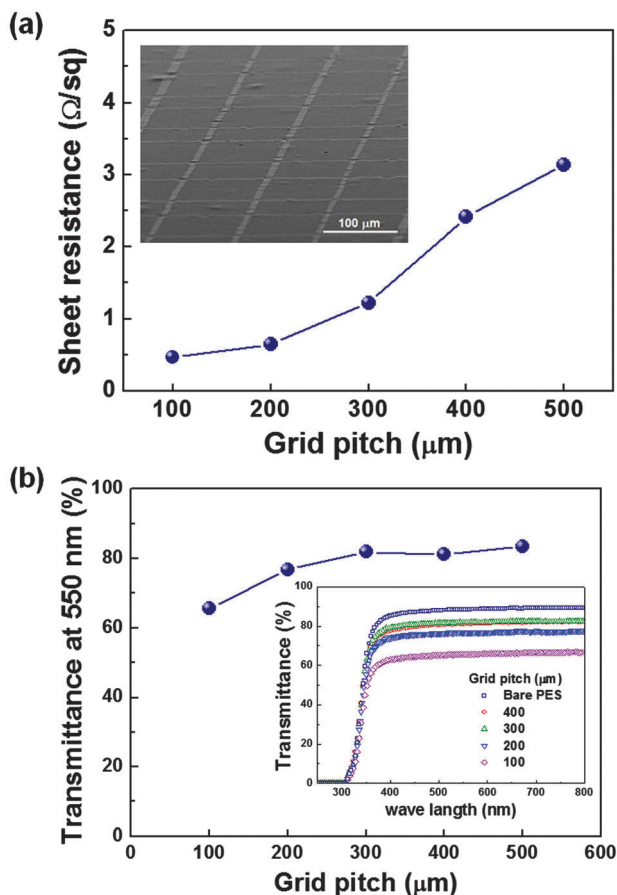


Fig. 4 (a) Sheet resistance of the thermal-pressed MGETE at different grid pitches. The inset shows a tilted SEM image of the MGETEs. (b) Optical transmittance of the MGETEs at 550 nm with different grid pitches. The inset presents the transmittance over a range of 300 nm to 800 nm.

Fig. 4 presents the electrical and optical properties of the MGETEs with different grid pitches. The substrate contribution is included in the optical transmittance measurement. **Both the sheet resistance and optical transmittance of the MGETEs decreased with a decrease of the grid pitch.** The optical transmittance remained above 80% for pitches wider than 300 μm (the bare PES films itself has the transmittance of 88% at 550 nm). The optical and electrical performance of the thermal-pressed MGETEs was evaluated by a figure of merit (FoM):<sup>38</sup>

$$\%T(\lambda) = \left(1 + \frac{188.5}{R_{sh}} \frac{\sigma_{OP}(\lambda)}{\sigma_{DC}}\right)^{-2}$$

where  $\sigma_{OP}(\lambda)$  and  $\sigma_{DC}$  are the optical conductivity at a wavelength of  $\lambda$  and the DC conductivity of the TE, respectively. The ratio of these conductivities,  $\sigma_{OP}(\lambda)/\sigma_{DC}$  is the definition of the FoM. A higher value of  $\sigma_{OP}(\lambda)/\sigma_{DC}$  indicates a desirable performance for the TE. The optical transmittance of the MGETEs with various pitches at a wavelength of 550 nm was plotted against their sheet resistance values in Fig. 5 (the other metal-grid works listed in Table 1 were also included). It should be noted that both transmittance values with and without the substrate contribution are used in Fig. 5. The FoM of the thermal-pressed MGETEs with

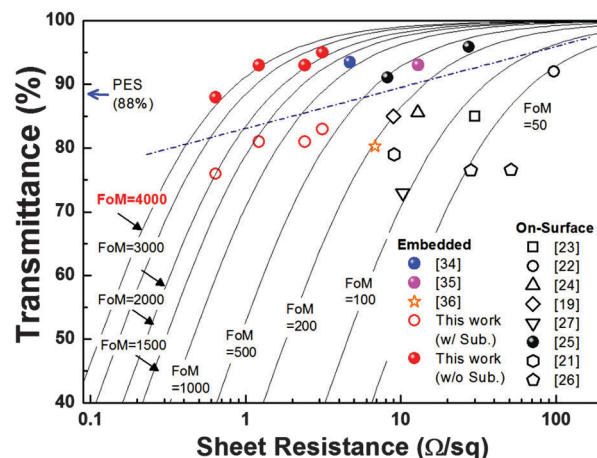


Fig. 5 The optical transmittance of the MGETEs in Table 1 at a wavelength of 550 nm plotted against their sheet resistance values.  $\sigma_{OP}(\lambda)/\sigma_{DC}$  indicates the FoM. Solid marks are for FoM values excluding the substrate contribution and open marks are for FoM values including the substrate contribution. (The transmittance of the PES substrate used in the work is 88%.)

a PES substrate ranges from 750 to 2000 as the metal-grid pitch varies from 500 μm to 200 μm. If the substrate contribution is disregarded, the value of the FoM increases above 4000. With and without the substrate contribution, the thermal-pressed MGETEs attest to superior performance as a TE compared to the other metal-grid TEs in Table 1, as well as other TEs, such as ITO (FoM  $\approx$  2000), graphene (FoM  $\approx$  120), and carbon nanotubes (FoM  $\approx$  30).<sup>35</sup>

The electromechanical stability of the thermal-pressed MGETEs was evaluated by measuring the post-bending change in the normalized resistance,  $(\Delta R/R_0)$ , where  $\Delta R$  is the actual change in the resistance after bending and  $R_0$  is the initial resistance. Fig. 6(a) shows the values of  $\Delta R/R_0$  at various bending radii under both **compressive (inner bending) and tensile (outer bending) stress conditions**. The inset shows the experimental setup for the bending test. The strain ( $\epsilon$ ) associated with a bending radius ( $r$ ) from 10 mm to 1 mm corresponds to the values from 1.2% to 12.5% calculated from  $\epsilon = h_s/(2r)$  where  $h_s$  is the substrate thickness (250 μm).<sup>39</sup> No significant increase in the resistance was observed up to 6.2% strain (3 mm bending radius) for both the compressive and tensile stress conditions. However, a strain greater than 12.5% led to a severe degradation of both stress conditions. The bending fatigue was also evaluated by monitoring  $\Delta R/R_0$  after multiple bending cycles at a radius of 10 mm, which corresponds to  $\epsilon = 1.2\%$ . Fig. 6(b) presents the  $\Delta R/R_0$  values after the bending cycle, indicating that the  $\Delta R/R_0$  values increase up to 30% and 62% of the original resistance of the thermal-pressed MGETEs after 1000 cycles under compressive and tensile stress conditions, respectively. The outcome of the bending test demonstrates a robust flexibility for the application of the thermal-pressed MGETEs in future flexible electronic devices.

The feasibility of the thermal-pressed MGETEs as TEs was confirmed by applying them in the fabrication of an inverted organic solar cell (IOSC). The pitch in the thermal-pressed

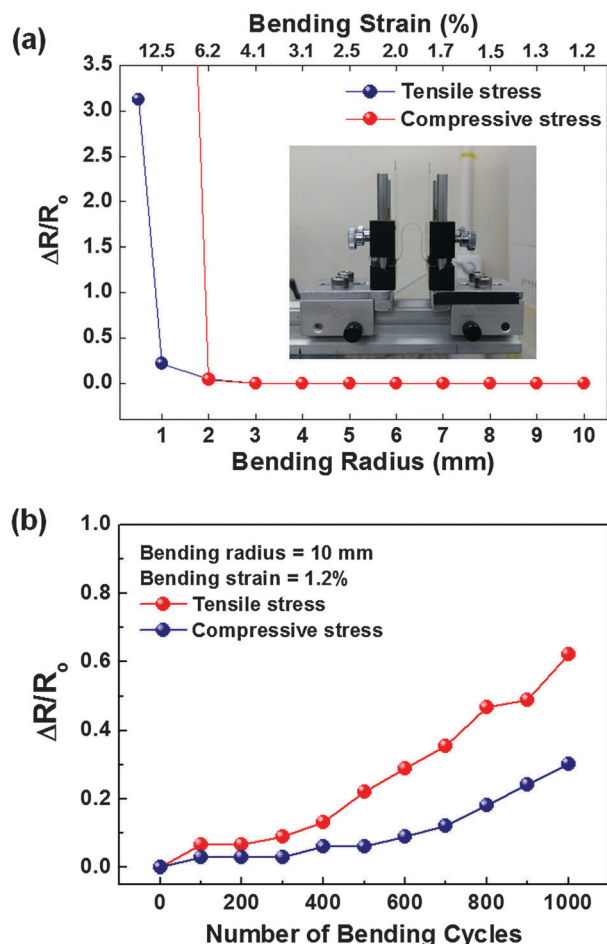


Fig. 6 (a)  $\Delta R/R_0$  at various bending radii under both compressive (inner bending) and tensile (outer bending) stress conditions and (b)  $\Delta R/R_0$  after the bending cycles (up to 1000 cycles).

MGETEs was fixed at 300  $\mu\text{m}$  for the fabrication of the IOSCs. A commercial poly(3,4-ethylenedioxythiophene) polystyrene sulfonate (PEDOT:PSS) solution (PH1000, Clevis) was spin-coated over the thermal-pressed MGETEs to cover the conductivity over the area between the metal-grid lines. Prior to annealing at 150  $^{\circ}\text{C}$  for 5 min, the PEDOT:PSS layer was treated with an ethylene glycol solution at a spinning speed of 5000 rpm for 40 s. Fig. 7(a) illustrates the device architecture of the IOSC consisting of a thermal-pressed MGETE with PH1000/ZnO/PTB-7:PC<sub>71</sub>BM/PEDOT:PSS/Ag. The photovoltaic performance of the IOSC on the thermal-pressed MGETE is presented in Fig. 7(b) and compared to the reference IOSCs, which were fabricated on commercial ITO glass (sheet resistance  $\sim 10 \Omega \text{ sq}^{-1}$  and  $\sim 90\%$  optical transmittance at 550 nm). To understand the influence of PH1000 on the power conversion efficiency (PCE), another IOSC was fabricated on a PH1000/PES plastic substrate without the metal-grid and showed a very poor device performance (PCE: 1%), indicating that the role of MGETE is more important for the IOSC performance. Table 2 presents the cell performance data, including short-circuit current density ( $J_{\text{sc}}$ ), open-circuit voltage ( $V_{\text{oc}}$ ), fill factor (FF), and PCE. There is no noticeable difference in  $V_{\text{oc}}$ , but a slightly lower value of  $J_{\text{sc}}$  in IOSC on the

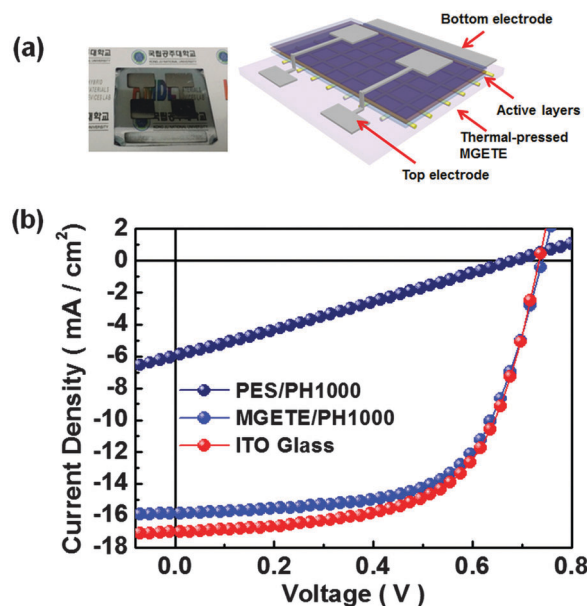


Fig. 7 (a) Device architecture of IOSCs consisting of a thermal-pressed MGETE with PH1000/ZnO/PTB-7:PC<sub>71</sub>BM/PEDOT:PSS/Ag and (b) photovoltaic performance of IOSCs on the thermal-pressed MGETE compared to the reference IOSCs on commercial ITO glass.

Table 2 IOSC performance data including the short-circuit current density ( $J_{\text{sc}}$ ), open-circuit voltage ( $V_{\text{oc}}$ ), fill factor (FF), and power conversion efficiency (PCE)

Transparent electrode for IOSCs	$V_{\text{oc}}$ (V)	$J_{\text{sc}}$ ( $\text{mA cm}^{-2}$ )	FF (%)	PCE (%)
PES/PH1000 ( $250 \Omega \text{ sq}^{-1}$ )	0.68	6.00	25.82	1.06
MGETE/PH1000	0.73	16.16	62.13	7.33
Commercial ITO glass	0.73	16.97	62.16	7.73

MGETE compared to the commercial ITO. The slightly low  $J_{\text{sc}}$  value could result from the lower transmittance of the MGETE (81% compared to 90% in ITO glass). The PCE of the IOSC on the thermal-pressed MGETE was 7.33%, which is very close to 7.73% obtained from the IOSC on commercial ITO glass. The flexibility of IOSCs on the thermal-pressed MGETEs was also investigated under compressive and tensile bending stress with various bending radii.

The PCE values at each bending radius were normalized to the initial PCE of IOSC and are shown in Fig. 8. There was no degradation up to a bending radius of 10 mm under both compressive and tensile stress conditions. However, the PCE continues to decrease down to 70% of its initial value under the compressive bending stress as the bending radius decreases to 3 mm. The IOSCs became inoperative at a bending radius below 2 mm. On the other hand, the IOSCs under a tensile bending stress deteriorated rapidly into a malfunctioning state even at a bending radius of 8 mm. We believe that such an abrupt decrease in the device performance comes from the degradation of the active layer of the IOSC under stress. The results of the bending test demonstrate that the thermal-pressed MGETEs could be accepted as promising TEs for future flexible electronic devices.

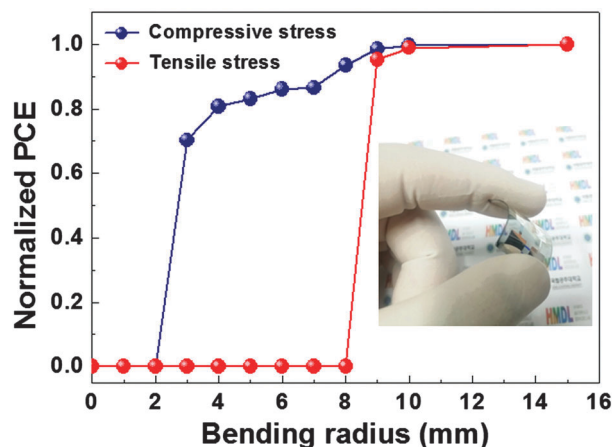


Fig. 8 PCE values at different bending radii. The PCE was normalized to the initial PCE of IOSC.

## Conclusions

Flexible MGETEs with a high aspect ratio and smooth surface were fabricated by thermal pressing of an EHD-printed metal-grid into plastic films. The thermal pressing process enhanced the sintering process, developing a dense microstructure in the metal-grid. The thermal-pressed MGETEs had a sheet resistance less than  $0.5 \Omega \text{ sq}^{-1}$  at an annealing temperature above  $200^\circ\text{C}$  and an optical transmittance above 80%, leading to an FoM of 2000. These characteristics indicate a superior performance for the thermal-pressed MGETEs compared to other pre-explored metal-grid TEs. The electromechanical stability of the thermal-pressed MGETEs was confirmed by measuring their post-bending change of normalized resistance, ( $\Delta R/R_0$ ) under both compressive and tensile stress conditions with various strain values. There was no degradation of  $\Delta R/R_0$  up to a 3 mm bending radius for both conditions, and a 30% and 62% degradation in  $\Delta R/R_0$  after 1000 cycles of compressive and tensile bending stress with a 10 mm radius, respectively. The IOSC built on the thermal-pressed MGETEs showed a PCE of 7.33%, comparable to the PCE of an IOSC on commercial ITO glass. There was no significant degradation in the post-bending device performance under a bending radius up to 10 mm. The excellent outcome of the bending test indicates a robust mechanical stability for the thermal-pressed MGETEs associated with flexibility for their application in future flexible electronic devices.

## Experimental

### EHD continuous jet printing of the metal-grid

A commercial EHD printer (ENJET NP-200), illustrated in Fig. S2 (ESI<sup>†</sup>), was used to prepare the metal-grid on the PES substrates whose size and thickness were  $25 \times 25 \text{ mm}^2$  and  $250 \mu\text{m}$ , respectively. The viscosity of a commercial Ag ink (NPK) was modified to 2000–4000 cPs by adding a polymer additive. This ink condition fits into a continuous jet mode, which forms a fine stream of ink from the nozzle. The nozzle used in the experiment was made of stainless steel with an inner diameter

of  $100 \mu\text{m}$ . The formulated ink was injected into the nozzle using a syringe pump at a feeding rate of  $150 \text{ nL min}^{-1}$ . The voltage applied to the nozzle with respect to the substrate was fixed at 1.5 kV. The nozzle was placed at 1 mm above the substrate during the entire printing process. The voltage elongated the ink stream, which enabled the fine patterning of Ag lines. The printing speed was controlled by the velocity of the stage (fixed at  $20 \text{ cm s}^{-1}$ ).

### Fabrication of thermal-pressed MGETEs

Two different buffer layers were stacked with PES substrates with the EHD-printed metal-grid—a glass plate placed on the surface where the metal-grid was printed and a PDMS film placed on the other side of the PES substrate (see Fig. 1). The smooth surface of the glass plate was used to uniformly press the entire metal-grid while the PDMS film was introduced to prevent the glass plate from being fractured during the pressing step. The stacked layers, consisting of glass/PES with metal-grid/PDMS, were placed in between two stainless steel plates. The mechanical pressing machine pressed down the entire layers (the pressing force was controlled by a computer program). An adjustable mounting clip then held the pressed sample together so that the applied pressure continued to be exerted over the entire layers. The clip-mounted sample was then moved into a box furnace for thermal pressing at various temperatures for 1 h.

### Fabrication and measurement of inverted organic solar cells

IOSCs were fabricated to assess the feasibility of the thermal-pressed MGETEs as a bottom electrode in the electronic devices. The device structure of the IOSC, electron selective layer/active layer/hole selective layer/Ag was built on the thermal-pressed MGETE and commercial ITO glass (Shinhan SNP Co. Ltd, sheet resistance  $\sim 10 \Omega \text{ sq}^{-1}$ ) as a reference. A highly conductive modified PEDOT:PSS (Clevios PH1000) was spin-coated over the MGETE to cover the conductivity where the metal-grid did not exist. Then an electron selective zinc oxide layer was spin-coated in sequence. The ZnO film (40 nm thick) was heat-treated at  $150^\circ\text{C}$  for 20 min in air. The ZnO sol-gel solution was prepared by dissolving zinc acetate (1.64 g, Aldrich) in 2-methoxyethanol (10 g, Aldrich) and then adding ethanolamine (0.5 g, Aldrich) to the solution. The final solution was stirred at room temperature for 1 h in an ambient environment. PTB7:PC<sub>71</sub>BM with a 1:1.5 mass ratio ( $8 \text{ mg mL}^{-1}$  PTB7 and  $12 \text{ mg mL}^{-1}$  PC<sub>71</sub>BM) was blended in chlorobenzene. The active-layer solution was filtered with a  $0.2 \mu\text{m}$  polytetrafluoroethylene syringe filter and then spin-coated onto the ZnO-coated MGETE. The thickness of the active layer was 90 nm. The PEDOT-PSS (Clevios P VP AI 4083) for the hole-selective layer was diluted in isopropyl alcohol (IPA) with a PEDOT-PSS:IPA ratio of 1:10. This hole-selective layer solution was spin-coated over the active layer at 5000 rpm for 40 s in a glove box. Finally, the Ag metal top electrode was deposited by thermal evaporation with a shadow mask, which defined the actual device area of  $0.38 \text{ cm}^2$ . The current density–voltage characteristics of the fabricated IOSCs were measured using a Keithley 2400 SourceMeter under simulated AM 1.5 illumination with a power density of  $100 \text{ mW cm}^{-2}$  (Oriol Sol 1A, Newport) that was calibrated using a standard Si photodiode detector fitted with a KG5 filter.



## Characterization

The line profile and the microstructure of the EHD-printed metal-grid were investigated using a surface profilometer (Veeco Dektak 150) and a focused-ion beam field emission scanning electron microscope (FIB FE-SEM; Nova 200), respectively. The electrical properties of the thermal-pressed MGETEs were monitored by four point probes (MST800C). The optical transmittance measurements were investigated using a UV/visible spectrometer (JASCO V-570) in the wavelength ranging from 300 nm to 800 nm.

## Acknowledgements

This work was supported by the Basic Science Research Program (NRF-2015R1D1A1A01058635) and the Nano R&D program (NRF-2015M3A7B4050307) through the National Research Foundation (NRF) and also supported by the Korea Institute of Energy Technology Evaluation and Planning (KETEP - No. 20153030012720).

## References

- 1 P. Blake, P. D. Brimicombe, R. R. Nair, T. J. Booth, D. Jiang, F. Schedin, L. A. Ponomarenko, S. V. Morozov, H. F. Gleeson, E. W. Hill, A. K. Geim and K. S. Novoselov, *Nano Lett.*, 2008, **8**, 1704–1708.
- 2 D. S. Hecht, L. Hu and G. Irvin, *Adv. Mater.*, 2011, **23**, 1482–1513.
- 3 T. H. Han, Y. Lee, M.-R. Choi, S. H. Woo, S. H. Bae, B. H. Hong, J. H. Ahn and T. W. Lee, *Nat. Photonics*, 2012, **6**, 105–110.
- 4 M. Bansal, R. Srivastava, C. Lal, M. Kamalasanan and L. Tanwar, *Nanoscale*, 2009, **1**, 317–330.
- 5 C. C. Chen, L. Dou, R. Zhu, C. H. Chung, T. B. Song, Y. B. Zheng, S. Hawks, G. Li, P. S. Weiss and Y. Yang, *ACS Nano*, 2012, **6**, 7185–7190.
- 6 J. Lee, P. Lee, H. Lee, D. Lee, S. S. Lee and S. H. Ko, *Nanoscale*, 2012, **4**, 6408–6414.
- 7 R. G. Gordon, *MRS Bull.*, 2000, **25**, 52–57.
- 8 M. A. Green, *Prog. Photovoltaics*, 2009, **17**, 347–359.
- 9 D. R. Cairns, R. P. Witte, D. K. Sparacin, S. M. Sachsman, D. C. Paine, G. P. Crawford and R. R. Newton, *Appl. Phys. Lett.*, 2000, **76**, 1425–1427.
- 10 F. C. Krebs, M. Jorgensen, K. Norrman, O. Hagenmann, J. Alstrup, T. D. Nielsen, J. Fyenbo, K. Larsen and J. Kristensen, *Sol. Energy Mater. Sol. Cells*, 2009, **93**, 394–412.
- 11 S. I. Na, S. S. Kim, J. Jo and D. Y. Kim, *Adv. Mater.*, 2008, **20**, 4061–4047.
- 12 M. W. Rowell, M. A. Topinka, M. D. McGehee, H. Prail, G. Dennler, N. S. Sariciftci, L. Hu and G. Gruner, *Appl. Phys. Lett.*, 2006, **88**, 233506.
- 13 G. Eda, Y. Y. Lin, S. Miller, C. W. Chen, W. F. Su and M. Chhowalla, *Appl. Phys. Lett.*, 2008, **92**, 233305.
- 14 J. Lee, S. T. Connor, Y. Cui and P. Peumans, *Nano Lett.*, 2008, **8**, 689–692.
- 15 D. S. Ghosh, L. Martinez, S. Giurgola, P. Vergani and V. Pruneri, *Opt. Lett.*, 2009, **34**, 325–327.
- 16 Y. Huang, F. Hsu, H. Cha, C. Chuang, C. Tsao and C. Chen, *Org. Electron.*, 2013, **14**, 2809–2817.
- 17 Y. Galagan, B. Zimmermann, E. W. C. Coenen, M. Jorgensen, D. M. Tanenbaum, F. C. Krieb, H. Gortler, S. Sabik, L. H. Slooff, S. C. Veenstra, J. M. Kroon and R. Andriessen, *Adv. Energy Mater.*, 2012, **2**, 103–110.
- 18 Y. Galagan, E. W. C. Coenen, S. Sabik, H. H. Gortler, M. Barink, S. C. Veenstra, J. M. Kroon, R. Andriessen and P. W. M. Blom, *Sol. Energy Mater. Sol. Cells*, 2012, **104**, 32–38.
- 19 Y. Jang, J. Kim and D. Byun, *J. Phys. D: Appl. Phys.*, 2013, **46**, 155103.
- 20 L. Hu, H. Wu and Y. Cui, *MRS Bull.*, 2011, **36**, 760–765.
- 21 J. Zou, H. L. Yip, S. K. Hau and A. K. Y. Jen, *Appl. Phys. Lett.*, 2010, **96**, 203301.
- 22 J. H. Park, D. Y. Lee, Y.-H. Kim, J. K. Kim, J. H. Lee, J. H. Park, T.-W. Lee and J. H. Cho, *ACS Appl. Mater. Interfaces*, 2014, **6**, 12380–12387.
- 23 S. Hong, J. Yeo, G. Kim, D. Kim, H. Lee, J. Kwon, H. Lee, P. Lee and S. H. Ko, *ACS Nano*, 2013, **7**, 5024–5031.
- 24 I. Kim, S.-W. Kwak, Y. Ju, G.-Y. Park, T.-M. Lee, Y. Jang, Y.-M. Choi and D. Kang, *Thin Solid Films*, 2015, **580**, 21–28.
- 25 Y. Jin, Y. Cheng, D. Deng, C. J. T. Qi, D. Yang and F. Xiao, *ACS Appl. Mater. Interfaces*, 2014, **6**, 1447–1453.
- 26 D. S. Ghosh, T. L. Chen and V. Pruneri, *Appl. Phys. Lett.*, 2010, **96**, 041109.
- 27 B. Murali, D.-G. Kim, J.-W. Kang and J. Kim, *Phys. Status Solidi A*, 2014, **211**, 1801–1806.
- 28 H. Wu, D. Kong, Z. Ruan, P.-C. Hsu, S. Wang, Z. Yu, T. J. Carney, L. Hu, S. Fan and Y. Cui, *Nat. Nanotechnol.*, 2013, **8**, 421–425.
- 29 B. W. An, E.-J. Gwak, K. Kim, Y.-C. Kim, J. Jang, J.-Y. Kim and J.-U. Park, *Nano Lett.*, 2016, **16**, 471–478.
- 30 J. Park and J. Hwang, *J. Phys. D: Appl. Phys.*, 2014, **47**, 405102.
- 31 K.-T. Park, J. Park, J.-W. Park and J. Hwang, *RSC Adv.*, 2015, **5**, 44847–44852.
- 32 B. W. An, B. G. Hyun, S.-Y. Kim, M. Kim, M.-S. Lee, K. Lee, J. B. Koo, H. Y. Chu, B.-S. Bae and J.-U. Park, *Nano Lett.*, 2014, **14**, 6322–6328.
- 33 M.-S. Lee, K. Lee, S.-Y. Kim, H. Lee, J. Park, K.-H. Choi, H.-K. Kim, D.-G. Kim, D.-Y. Lee, S. Nam and J.-U. Park, *Nano Lett.*, 2013, **13**, 2814–2821.
- 34 Y. S. Oh, D. Y. Choi and J. J. Sung, *RSC Adv.*, 2015, **5**, 64661–64668.
- 35 S. Jung, S. Lee, M. Song, D.-G. Kim, D. S. You, J.-K. Kim, C. S. Kim, T.-M. Kim, K.-H. Kim, J.-J. Kim and J.-W. Kang, *Adv. Energy Mater.*, 2014, **4**, 1300474.
- 36 J.-S. Yu, G. H. Jung, J. Jo, J. S. Kim, J. W. Kim, S.-W. Kwak, J.-L. Lee, I. Kim and D. Kim, *Sol. Energy Mater. Sol. Cells*, 2013, **109**, 142–147.
- 37 S. K. Vishwanath, D.-G. Kim and J. Kim, *Jpn. J. Appl. Phys.*, 2014, **53**, 05HB11.
- 38 M. G. Dressel and G. Gruner, *Electrodynamics of solids: optical properties of electrons in matter*, Cambridge University Press, Cambridge, 2002.
- 39 S.-I. Park, J.-H. Ahn, X. Feng, S. Wang, Y. Huang and J. A. Rogers, *Adv. Funct. Mater.*, 2008, **18**, 2673–2684.